Phase Variations and Layer Epitaxy of 2D $PdSe_2$ Grown on 2D Monolayers by Direct Selenization of Molecular Pd Precursors

Kuo Lun Tai,[1,2] *Jun Chen,*[1] *Yi Wen,*[1] *Hyoju Park,*[3,4] *Qianyang Zhang,*[1] *Yang Lu,*[1] *Ren-Jie Chang,*[1] *Peng Tang,*[1] *Christopher S. Allen,*[1,5] *Wen-Wei Wu,*[*,2,6] *and Jamie H. Warner*[*,3,4]

[1]Department of Materials, University of Oxford, Parks Road, Oxford OX1 3PH, United Kingdom

[2]Department of Materials Science and Engineering, National Chiao Tung University, Hsinchu 300, Taiwan (R.O.C.)

[3]Walker Department of Mechanical Engineering, The University of Texas at Austin, 204 East Dean Keeton Street, Austin, Texas, 78712, United States

[4]Materials Graduate Program, Texas Materials Institute, The University of Texas at Austin, 204 East Dean Keeton Street, Austin, Texas, 78712, United States

[5]Electron Physical Sciences Imaging Center, Diamond Light Source Ltd., Didcot, Oxfordshire OX11 0DE, United Kingdom

[6]Center for the Intelligent Semiconductor Nano-system Technology Research, National Chiao Tung University, Hsinchu 300, Taiwan

*email: Jamie.warner@austin.utexas.edu; wwwu@mail.nctu.edu.tw

Abstract

2D materials and van der Waals heterostructures with atomic-scale thickness provide enormous potential for advanced science and technology. However, insufficient knowledge of compatible synthesis impedes wafer-scale production. $PdSe_2$ and Pd_2Se_3 are two of the noble transition-metal chalcogenides with excellent physical properties that have recently emerged as promising materials for electronics, optoelectronics, catalyst, and sensor. This research presents a feasible approach to synthesize $PdSe_2$ and Pd_2Se_3 with inherently asymmetric-structure on honeycomb lattice 2D monolayer substrates of graphene and MoS_2. We directly deposit a molecular transition-metal precursor complex on the surface of the 2D substrates, followed by low-temperature selenization by chemical vapor flow. Parameter control leads to tuning of the material from monolayer nanocrystals with Pd_2Se_3 phase, to continuous few-layer $PdSe_2$ films. Annular dark-field scanning transmission electron microscopy (ADF-STEM) reveals the structure, phase variations and heteroepitaxy at the atomic level. $PdSe_2$ with unconventional interlayer stacking shifts appeared as the kinetic product, whereas the bilayer $PdSe_2$ and monolayer Pd_2Se_3 are the thermodynamic product. The epitaxial alignment of interlayer rotation and translation between the $PdSe_2$ and underlying 2D substrate were also revealed by ADF-

STEM. These results offer both nanoscale and atomic-level insights into direct growth of van der Waals heterostructures, as well as an innovative method for 2D synthesis by predetermined nucleation.

Keywords: $PdSe_2$, 2D materials, graphene, TEM, Pd_2Se_3, MoS_2

In this digital age, the semiconductor technology has revolutionized human lives, which stems from the application of silicon wafer grown by the Czochralski process.[1] For the past two decades, semiconductor fabrication is approaching the scaling limit due to the short channel effect and unbearable heat dissipation.[2] A consensus on the incorporation of promising materials or advanced transistor structure has emerged.[3] Since the debut of experimentally-extracted monolayer graphene, considerable research studies have been dedicated to 2D materials.[4] With an atomically-thin thickness, 2D materials and its derivative van der Waals heterostructures manifest dangling-bond-free surfaces and synergistic interface effects that have plagued the 3D bulk materials.[5]

The potential applications of 2D materials also exist in non-computational systems beyond the modern Si electronic, such as photodetectors, image sensors, data communication technology, and gas/chemical/biological detection.[3, 6] A wide range of fundamental properties and improved device performance have already been implemented through the integration of semimetal graphene, semiconductor transitional metal dichalcogenides (TMDs), insulator h-BN and their vertical or lateral heterostructures.[7-14] Recently, the research interests has expanded to include noble-transition-metal dichalcogenides (NTMDs), group-IVA elemental Xenes and their monochalcogenides, Gallium and Indium chalcogenides, 2D oxide layers, 2D perovskites insulators, 2D superconductors and topological insulators, and van der Waals heterostructures.[6, 9, 15-19] Among these, the group-10 NTMDs such as $PtSe_2$ and PtS_2 distinguish themselves as the emerging 2D semiconductors with adequate carrier mobility, long-term air stability, and strong interlayer coupling.[20] $PdSe_2$ is one of the NTMDs with the predicted bandgap of 1.3 eV (monolayer) to 0.03eV/0 eV (3D bulk), and exhibited ambipolar carrier conduction and metal-insulator transition, rendering it a promising candidate for future electronic and optoelectronic application.[21-25] In comparison with the Xenes (silicene, germanene, and stanine) and phospoerene, few-layer $PdSe_2$ has a similar buckled or puckered structure that breaks the sublattice symmetry, yet with high air stability. Moreover, unlike most conventional 2D materials, $PdSe_2$ has an inherent structure of pentagonal bonding and the 4-fold coordination of Pd atoms, often described as the Pd-backbone square network.[26, 27] More specifically, the Pd atom coordinates with four Se atoms and an intralayer Se-Se dumbbell bonding cross the Pd layer. This 2D puckered pentagonal structure with low–symmetry sets the stage for future piezoelectric, spintronic and valleytronic applications.[28, 29] As most studies have demonstrated the preferable presence of a minimum unit of bilayer $PdSe_2$, many of which have questioned the physical existence of monolayer $PdSe_2$.[27] Monolayer Pd_2Se_3 has then come to notice because it was frequently produced in the Se-loss thinning process driven by an electron beam.[27, 30] It is an emerging 2D thermoelectric material that shows higher efficiency than other monolayer TMDs.

With its predicted band bap of 0.45 eV and carrier mobility of 178.02 $cm^2V^{-1}s^{-1}$, Pd_2Se_3 is expected to show excellent anisotropic transport properties and a pronounced optical absorption in the entire solar spectrum, making it a promising material for optoelectronic devices.[31-33]

Despite a wealth of fascinating functions afforded by 2D materials, the development of scalable synthesis that can coexist with CMOS technology is at its infancy.[34] The grand challenges include the growth at compatible temperature, seeing that the conventional chemical vapor deposition (CVD) system requires a high temperature around 600-900 ℃.[35-37] The direct-growth or one-step growth methods should also be established, since the prevailing 2D van der Waals heterostructures are predominantly mechanically-assembled,[5, 9, 15] while this is non-standard in microelectronic fabrication. Research on $PdSe_2$ and Pd_2Se_3 has highlighted the enhanced device performance, some of which were based on mechanical exfoliation with substantial properties, while others utilized top-down patterning either by plasma or laser to create heterophase contacts by phase transformation.[38-41] On the other hand, structural dynamics and 1D channel-etching have been thoroughly investigated at the atomic level using annular dark-field scanning transmission electron microscope (ADF-STEM) imaging with the *in situ* heating setting.[30, 42] Although a few studies have been devoted to synthesis, these research are either limited by the incompatible temperature (>400℃) or the inadequate coverage and continuity,[21, 25, 43-46] rather less attention has been paid to the insights of growth in terms of nucleation, growth kinetics, and substrate impact.[34, 47]

Analogous to the idea of using the seed crystal for Si wafer and the dip-coating method for 2D MoS_2,[1, 48] we demonstrated herein the use of transition-metal allyl complex as precursors, which were pre-dispersed on the growth substrate before selenization, to grow the few-layer 2D crystals. The low-temperature ambient-pressure CVD system was employed to comply with the temperature for the existing CMOS fabrication. By adjusting the concentration and growth time, we achieved the growth of continuous film qualitatively equivalent to the commercial sample, substantiated by Raman analysis and STEM imaging. The use of 2D-material substrate suspended on TEM grids along with ADF-STEM imaging enable us to capture the phase variations as well as heteroepitaxial alignment at the atomic level.

Results and Discussion

Drop-casting is a facile and tunable deposition method for spreading monolayers and thin films of nanoparticles over a substrate (~1cm^2). Generally, the distribution on substrates can be varied by the volume of dispersion and the particle concentration, given the desirably volatile solvents and wetting conditions. This paper uses the drop-casting method and demonstrates the role of Allylpalladium (II) chloride dimer as the precursors for palladium selenide growth, in contrast to its extensive use as a catalyst. A polar aprotic solvent, 1, 2-Dichloroethane, was selected for greater volatility and solubility. The precursor solutions were sonicated to agitate particles for ideal dispersion. Graphene is chosen as the suspended substrates because of its high electron transparency and the prevalence in the construction of van der Waals heterostructures.[49] Monolayer MoS_2 was also used as the 2D substrate to show the broader viability of the methods.

Figure 1a shows the schematic of the experimental procedure. The same volume of dispersion was drop-casted on TEM grids that had suspended graphene on top of the observation membrane. The SiNx membrane was fully covered by graphene, and its area is 0.50 mm x 0.50 mm with 2 μm vacuum pores spaced 5 μm apart. Figure 1b shows the ADF-STEM image of the deposited precursors with nanometer-size on graphene on a TEM grid. The particles with dimmer contrast represent the thinner and smaller precursors, whereas those with brighter contrast are the thicker and larger precursors. The higher magnification ADF-STM image in Figure 1c shows the atomic structure of these palladium particles. Fig 1d shows the two furnace settings for selenization. The CVD system was first flushed with 500 sccm of Ar gas for 30min, and then both furnaces were heated at a rate of 15 ℃/min until both furnaces reached at targeted temperature, Zone 1 at 240 ℃ and Zone 2 at 360 ℃. After one-hour selenization, Zone 2 was first cooled down to 240℃, and then both furnaces were shut down for rapid cooling; this ensured the selenium-rich environment during growth. Figure 1e-f present the product after selenization, where the nanoparticles was transformed into the veined crystal, and the atomic structure shows feathery $PdSe_2$ lattice. From the scattered Pd nanoparticle form of precursor to the connected veined morphology, the growth indicated the probability of film implementation.

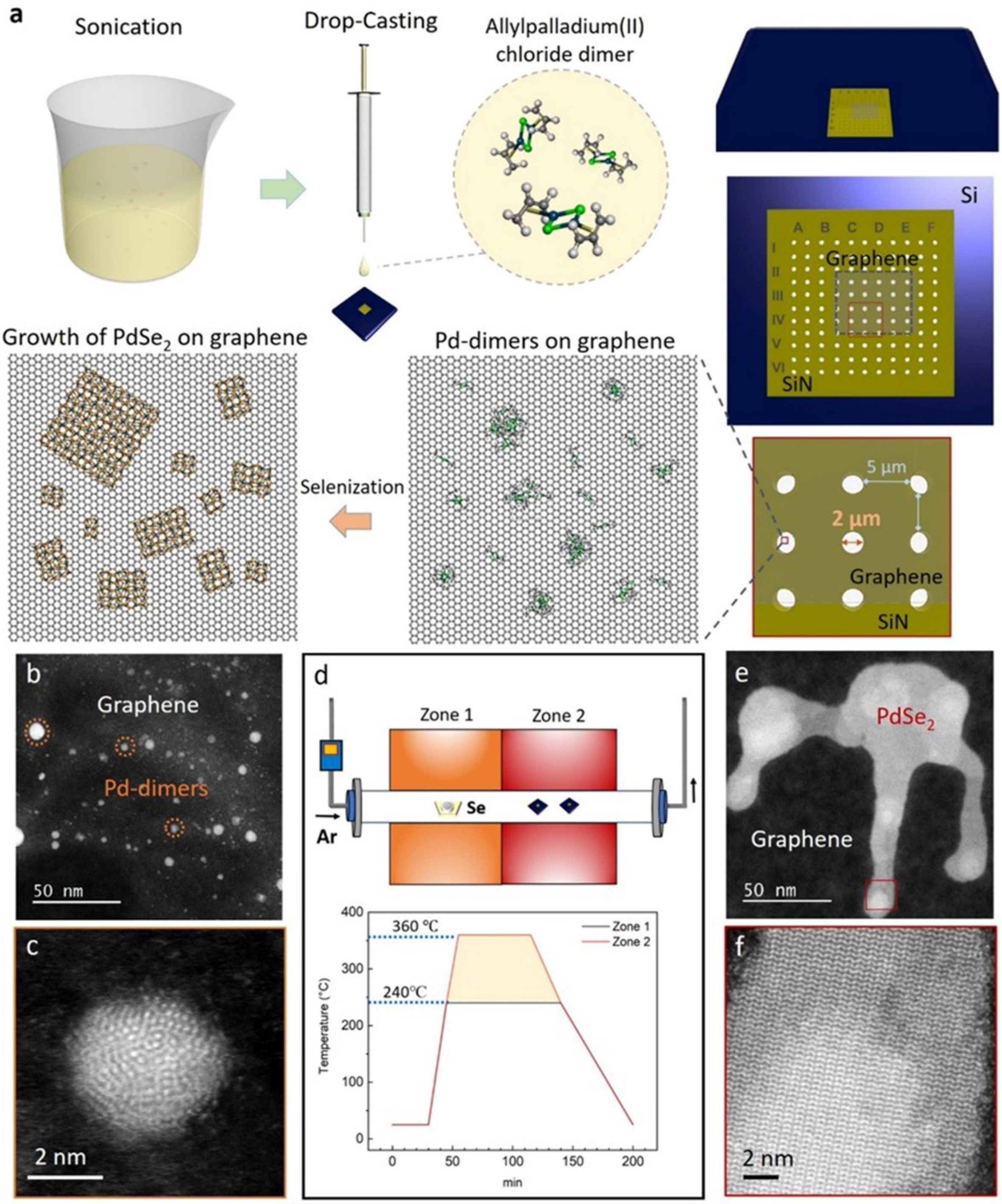

Figure 1. Synthesis of PdSe$_2$ domains on graphene by selenization of allylpalladium chloride dimer. (a) Schematic illustration of experimental settings. (b) Low-magnification ADF-STEM image of Pd-dimer drop-casted on graphene. (c) ADF-STEM image of a single nanocluster of Pd-dimers. (d) Schematic illustration of furnace settings and temperature profile. (e) Low-

magnification ADF-STEM image of single $PdSe_2$ domain. (f) Atomic-resolution ADF-STEM image showing the structure of bilayer pentagonal $PdSe_2$.

Varying the solution concentration leads to different particle number and size per volume unit, which then alters the distribution of precursors on the substrate. We carried out experiments at four different millimolar concentrations of 0.1 mM, 1 mM, 8 mM, 20 mM, respectively. Fig S1-S4 showed the ADF-STEM images of the precursor distribution for each concentration before selenization. By keeping all the other growth parameters fixed, including the gas flow, the substrate distance, and the growth duration (1hr), the growth results were concentration-dependent. Figure 2a-h show the ADF-STEM images at different magnifications, comparing the growth coverage of these four concentrations. The 0.1 mM in Figure 2a,e show nanoflake formation with relatively thin thickness. We measured the size by Feret Diameter and calculated the number of nanoflakes in each size range. Figure 2i shows the size distribution with Gaussian fitting, suggesting that most of the nanoflakes were 2-6 nm in size while the size ranged from 0.5nm to 18 nm. The 1 mM sample in Figure 2b,f show the limited growth with a localized connected morphology, which resulted from its innate precursor localization (Figure S2). Figure 2k measured the intensity profile of the region in the 1mM sample, showing a steep thickness gradient from the graphene substrate (0L) to 8L. In contrast, the 8 mM sample in Figure 2c,g shows an extensively continuous film morphology, derived from the even distribution of uniform precursors (Figure S3). The 20 mM sample (Figure 2d,h), on the other hand, shows a reverse bulky growth, where the oversaturated seeds in the environment could favor the bulk growth rather than the film expansion (Figure S4 and Figure S5d). Figure 2j presents the statistics of growth coverage with 8mM reached the highest point at 90%, whereas the lowest number was seen in 0.1mM at 8.69%. In short, the growth coverage relates to the plantation and the degree of saturation of precursors.

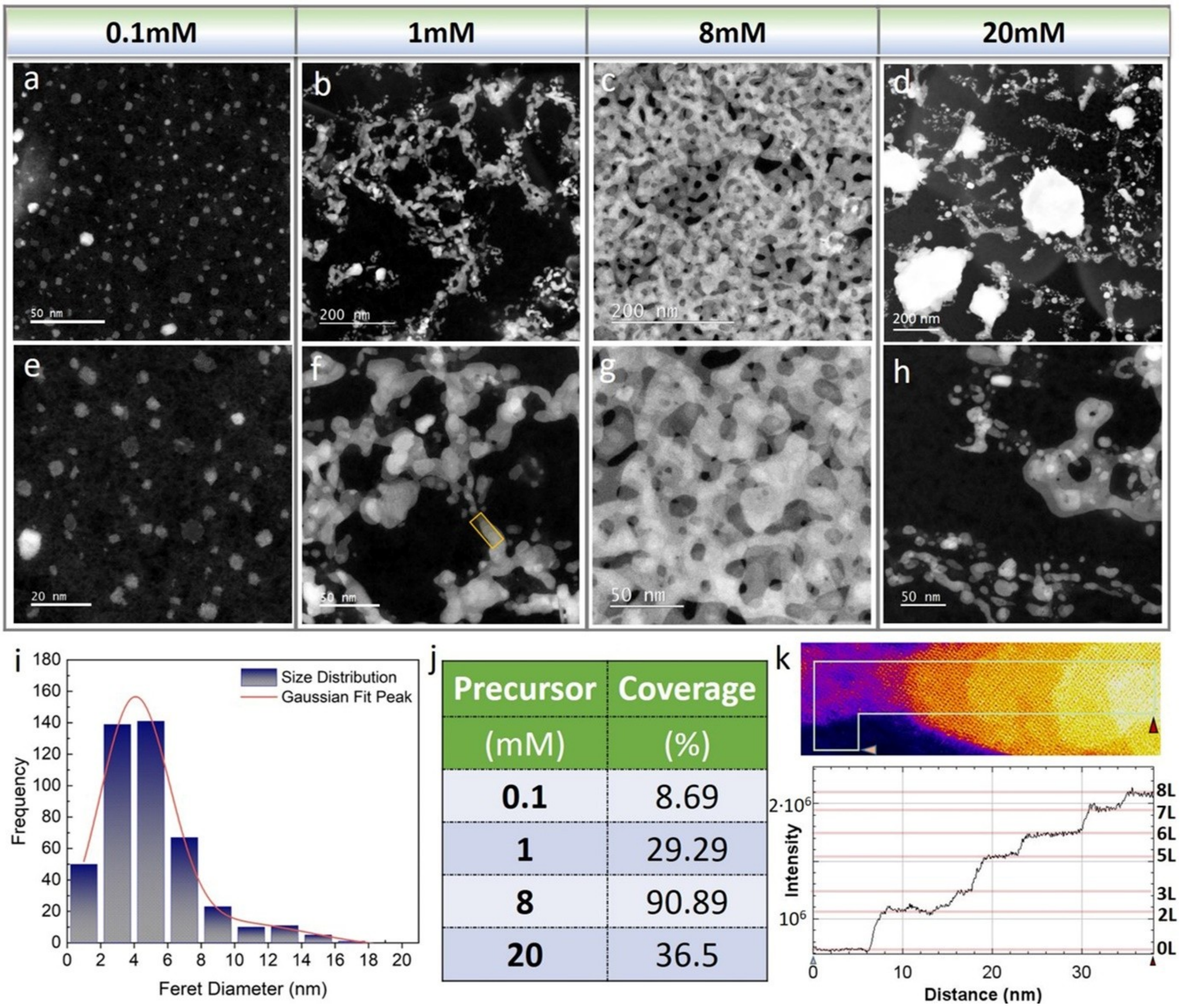

Precursor (mM)	Coverage (%)
0.1	8.69
1	29.29
8	90.89
20	36.5

Figure 2. The precursor-concentration-dependent growth of 2D Palladium selenide. (a-d) ADF-STEM images showing the growth results from different concentrations of 0.1mM, 1mM, 8mM, and 20Mm, respectively. (e-h) ADF-STEM images showing the higher magnification of images corresponding to each concentration growth results. (i) The statistical distribution of the

nanoflakes in size in 0.1mM. (j) Coverage calculation of different precursor concentration. (k) Line intensity profile showing the thickness variation of the 1mM sample.

Phase determination for these synthesized nanostructures is necessary as several phases of palladium selenide have been proven stable in ambient conditions. We further investigated the atomic structures using atomic resolution ADF-STEM imaging. The images in Figure 3a-b were obtained from the 0.1mM sample and the 8 mM sample, respectively. Figure 3c-g show the atomic structures of nanoflakes, manifesting that the nanoflakes were monolayer $Pd_2Se_{3,}$ where the experimental images and corresponding Fast Fourier transformation (FFT) accorded with the simulation data. Figure 3h-l show the atomic structures of film, the experimental images and corresponding FFT also agreed well with simulation data, demonstrating that the films consisted of $PdSe_2$. The growth features corresponding to 1 mM and 20 mM were shown in Figure S5. It is worth noting that in Figure 3a, the nanoflakes were composed of not only monolayer Pd_2Se_3 but also bilayer $PdSe_2$, inferring that monolayer Pd_2Se_3 was thermodynamically favorable in the monolayer Pd-Se system, albeit in Se-sufficient environment. This result echoes the recent studies that monolayer Pd_2Se_3 is more physically-stable than monolayer $PdSe_2$.

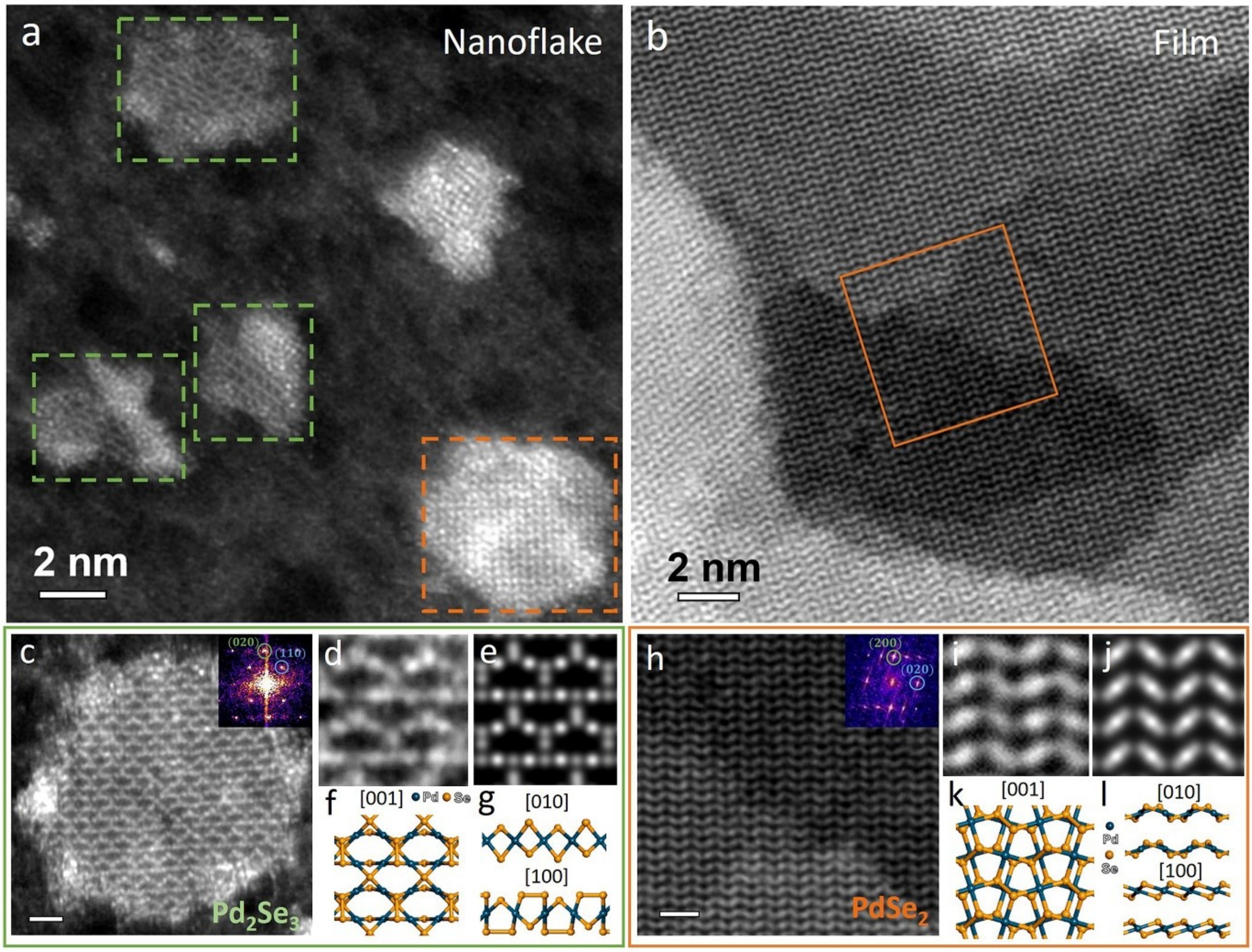

Figure 3. Atomic structures and schematic illustration of continuous 2D few-layer $PdSe_2$ and monolayer Pd_2Se_3. (a) ADF-STEM image showing the growth condition of 0.1mM-sample consisting of $PdSe_2$ and Pd_2Se_3 nanoflakes, where $PdSe_2$ and Pd_2Se_3 marked by the orange dot line and green dot line, respectively. (b) ADF-STEM image of 8mM-sample showing the structure of continuous few-layer $PdSe_2$. (c) ADF-STEM image from 0.1mM-sample. The scale bar: 1nm. (d) Experimental ADF-STEM image of atomic structures of Pd_2Se_3. (e) Multislice simulated ADF-STEM image and (f-g) corresponding atomic models of Pd_2Se_3 viewed from [001], [010], and [100]. (h) The magnified image marked by the orange box of (b). The scale bar: 1nm. (i) Experimental ADF-STEM image of atomic structures of $PdSe_2$. (j) Multislice simulated ADF-

STEM image and (k-l) corresponding atomic models of $PdSe_2$ viewed from [001], [010] and [100].

The epitaxy between the monolayer nanoflakes grown with 0.1mM precursor concentration and the underlying graphene support was explored in Fgure 4. The graphene lattice was imaged next to the Pd_2Se_3, because the strong contrast from the Pd_2Se_3 prevents graphene from being detected underneath. The majority of the Pd_2Se_3 monolayers were aligned to the graphene, confirming epitaxy, as illustrated in Fgure 4. This is expected for direct growth of one 2D material on the surface of another. In addition, we concurrently captured the single crystal form of $PdSe_2$ and monolayer Pd_2Se_3 in the 0.1M sample (Figure 3-4), contrasting sharply with the

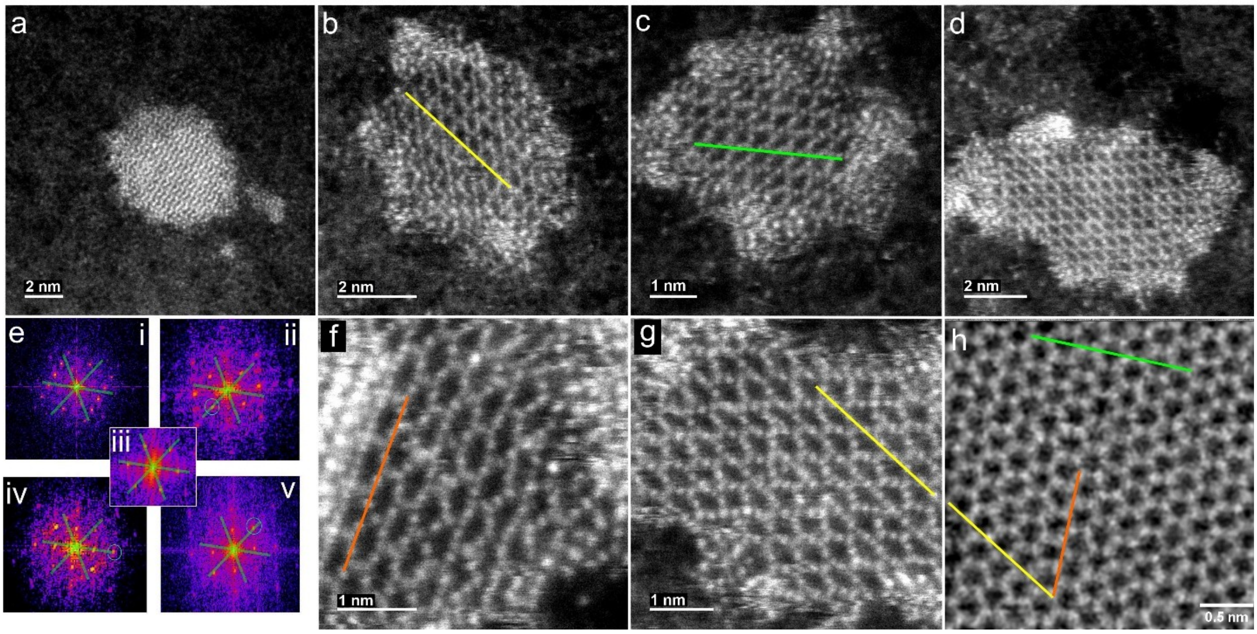

Pd_2Se_3 that formed within $PdSe_2$ matrix by electron beam irradiation or thermal annealing (Figure S6).

Figure 4. ADF-STEM of 0.1mM precursor growth on graphene. (a) $PdSe_2$ nanoflake, (b)-(d) Pd_2Se_3 nanoflakes from the same local region on graphene. (e) FFTs taken from (i) panel (a), (ii) panel (b), (iii) panel (h) graphene, and (iv) panel (c), and (v) panel (d). (f), (g) High magnification ADF-STEM images of two different Pd_2Se_3 monolayers showing lattice alignment to (h) ADF-STEM image of graphene located next to these domains.

Time-variant experiments allow us to evaluate the timescale for film growth. Considered the thermal budget (below 400℃) for integrating the 2D materials into the silicon-integrated circuits, this study kept the selenization temperature at 360℃, although the higher temperature could shorten the timescale. Figure 5 shows the growth results of the 8mM samples given different selenization time, at 15 min, 45 min, 60 min, and 60 min-2nd drop. In Figure 5a-h, the film coverage increased as the growth time increased, whereas the area of chunks (immature seeds) reduced as the growth period prolonged. The film and chunk coverage was shown statistically in Figure 5l. The 60 min sample in Figure 5c,g has shown the complete film formation with coverage of 88.19%. The 2nd drop was then applied to this sample and was selenized for another 60 min, showing an enhanced coverage of 98.16%. Low-magnification images in 5i-j, typical Raman signals of few-layer $PdSe_2$ in Figure 5k and Figure S7 and energy-dispersive X-ray (EDX) spectrum in Figure S8 illustrated the film realization at the micron scale. The atomic resolution image displayed in Figure 5q also shows a feathery few-layer $PdSe_2$ lattice.

It is evident that the films grown by our method are comparable to the commercial sample, as displayed in Figure S9. Figure 5m-p show atomic structures and corresponding FFT around the seeds in the 15 min sample. The area adjacent to the seed showed Pd_2Se_3 lattice viewed from zone axis [111], corroborated by simulation in Figure S10. The region further away from the seed shows typical bilayer $PdSe_2$ lattice and FFT, while the lattice of immature seeds (Pd_xSe_y) with higher contrast fail to reach an atomic resolution due to its thickness and disorder.

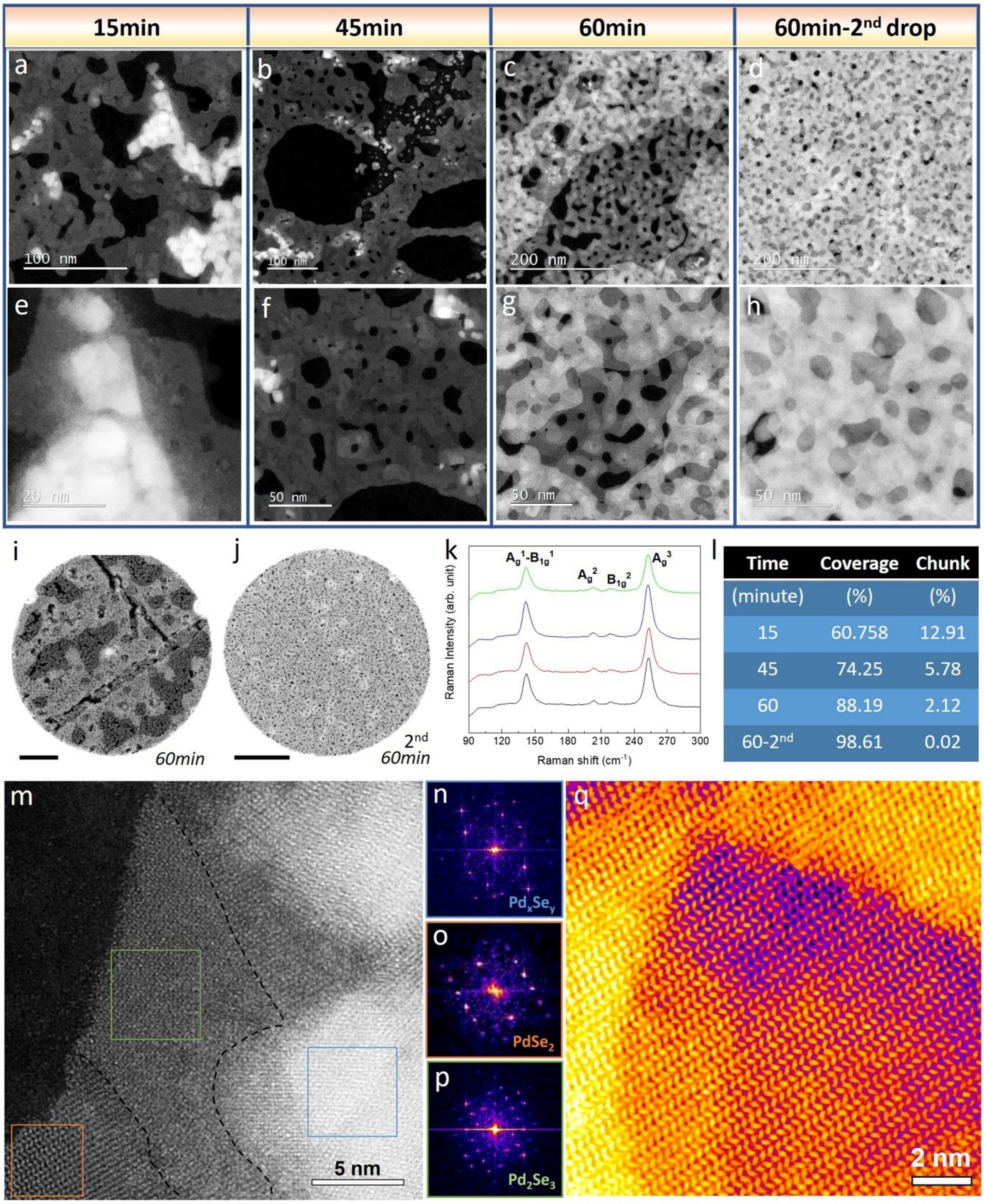

Time (minute)	Coverage (%)	Chunk (%)
15	60.758	12.91
45	74.25	5.78
60	88.19	2.12
60-2nd	98.61	0.02

Figure 5. Tuning the growth duration of 8mM and applying the second drop to grow nearly full coverage few-layer $PdSe_2$. (a-d) ADF-STEM images showing the growth results with different growth duration of 15min, 45min, 60min, and another 60min growth after the second drop. (e-h) ADF-STEM image showing higher magnification images corresponding to

(a)-(d). (i) Low-magnification ADF-STEM images of the film coverage of 8mM-sample of 60-min growth at micron-scale. (j) Low-magnification ADF-STEM images of the film coverage of secondary selenization of (i) at micron-scale. (k) Consistent few-layer $PdSe_2$ of Raman spectrum obtained from four different areas with 5 μm intervals. (l) Statistics of film coverage and chunk percentage. (m-p) ADF-STEM image of the 15 min sample showing the region near the palladium source and FFT from square areas marked in different colors. (q) ADF-STEM image showing the atomic structures of the 60min 2nd-drop sample.

Next, we examine the atomic structures of the 15 min sample, as short reaction time can reveal the kinetic phases. Unlike the normally expected $PdSe_2$ lattice, the lattice structure in Figure 6a arranged in a rather inconsistent manner; this implied the presence of other phases established in the Pd-Se phase diagram. However, as we looked into other phases in terms of crystal structure and atomic arrangement, all phases were three-dimensional crystal systems except layer-structured $PdSe_2$ and Pd_2Se_3 (Figure S11). The Inset FFT in Figure 6a of the whole region indicated a certain epitaxial 2D heterophase stacking within this layered structure. For direct comparison, Figure 6b exhibits the simulated diffraction pattern corresponding to monolayer $PdSe_2$, bilayer $PdSe_2$, and Pd_2Se_3. It should be mentioned that monolayer $PdSe_2$ and bilayer $PdSe_2$ adopt different crystal systems due to their symmetry (Figure S12), with the former belonged to the monoclinic (M-$PdSe_2$) while the latter classified as the orthorhombic (O-$PdSe_2$). The d-spacing of the principal diffraction spots (020) and (200) from these three structures show marginal difference; however, we can clearly see the difference from the diffraction patterns. That is, the M-$PdSe_2$ shows a square pattern but losses the inner low-index spots compared with the other two. On the other hand, the O-$PdSe_2$ shows a rectangular pattern with larger spacing, while the Pd_2Se_3 exhibits an unequal hexagonal pattern of its principal low-index spots. Therefore, the heterophase can be determined preliminarily through the identification of diffraction patterns. A case of the FFT in Figure 6a exhibits the epitaxial stacking of M-$PdSe_2$ and $Pd_2Se_{3,}$ noted that no rotational stacking pattern appeared. We can then extrapolate that the discrete lattice in the 15 min sample resulted from the translational stacking of $PdSe_2$ and Pd_2Se_3 layers. Figure 6i-k categorized three diffraction patterns we found in Figure 6a, with the type I, II, III corresponding to the heterophase stacking M-$PdSe_2$, Pd_2Se_3/M-$PdSe_2$, and Pd_2Se_3/M-$PdSe_2$/O-$PdSe_2$, respectively. Other areas in the 15min sample also showed these three dominant diffraction patterns (Figure S13). Then the translations between these layers were further examined using Z-contrast ADF-STEM imaging and multislice image simulation. Figure 6c displays a limited area with a typical M-$PdSe_2$ pentagonal lattice. In comparison to the inherent O-$PdSe_2$ bilayer stacking, this showed the AA stacking bilayer confirmed by Figure 6d-g and Figure S14. Next, Figure 6l shows the image with a higher magnification of Type I with its M-$PdSe_2$ type diffraction pattern (Figure 6m). As the atom-resolved image shown in Figure 6n, the sublattice shows no symmetry but a periodic unit, suggesting the translational alignment in the x-y plane by monolayers M-$PdSe_2$. By disassembling it layer-by-layer, Figure 6n-v shows the structure consisted of three M-$PdSe_2$ monolayers. The reference points were marked in Figure 6q-v to determine the absolute position, which often considered as Pd-backbone in the interlayer stacking mechanism. More specifically, the 2nd layer shows a translation toward the Ⅰ quadrant, whereas the 3rd layer shows a translation toward the Ⅳ quadrant. The Se atoms with different coordination of both layers located on top of the Pd atom at the reference points.

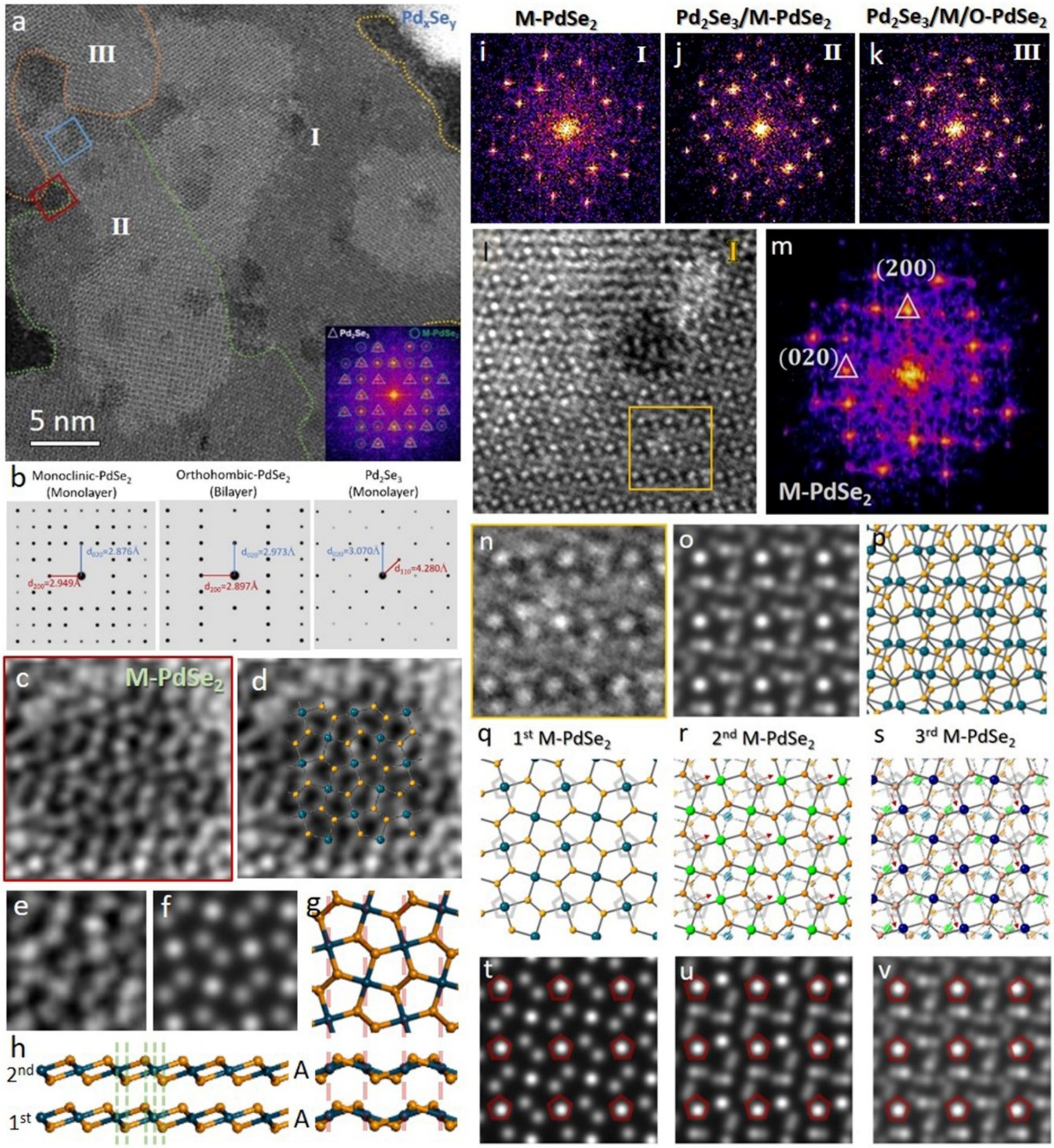

Figure 6. Revealing the evolutionary phases during growth through cutting the growth time down to 15min. (a) ADF-STEM image showing the region adjacent to the palladium Inset is the corresponding FFT of the whole region, wihich was realigned vertically. (b) Simulated Single crystal diffraction patterns corresponding to different palladium selenide phases. (c-h) A bilayer monoclinic $PdSe_2$ (M-$PdSe_2$) structure. (c) The experimental ADF-STEM image. (d) The image with the atomic model for clear vision. (e) Magnified view of (c). (f) Simulated image and the corresponding atomic model (g). (h) The side-view atomic model. (i-k) FFT of regions divided in (a). (l-v) The translational symmetry of M-$PdSe_2$ stacked trilayer. (l) ADF-STEM image showing the region I and (m) corresponding FFT. (o) The magnified experimental image shows a trilayer M-$PdSe_2$ with interlayer shifts. (p) The simulated image and the corresponding atomic model. (q-s) Layer-by-Layer atomic model showing the stacking configuration and corresponding simulated images (t-v).

In Figure 7, we analyzed the atomic structures of type II and type III. The ADF images of type II (Figure 7a-b) show that a specific Moiré pattern resulted from the stacking of Pd_2Se_3 and $PdSe_2$. 2D FFT (Figure 6j) indicates the heteroepitaxy of monolayer Pd_2Se_3 and M-$PdSe_2$ with its crystallographic relation of $(020)_{Pd2Se3}$ // $(020)_{M\text{-}PdSe2}$. The (200), (210), (220) for M-$PdSe_2$ and (110) for Pd_2Se_3 are easily identified. However, the interplanar spacing of $(020)_{Pd2Se3}$ and $(020)_{M\text{-}PdSe2}$ are very close, 0.307 nm for $(020)_{Pd2Se3}$ and 0.287 nm for $(020)_{Pd2Se3,}$ these two diffraction spots overlap with each other. We further carried out multislice ADF-STEM simulation based on the atomic model (Figure 7d-e), which provide the similar Moiré pattern and agree well with the experimental ADF-STEM image (Figure 7c). Figure 7f-h illustrate the interlayer atomic distance using Pd atoms as reference points; this enables us to clarify the lattice configuration from the top view. The $\Delta\delta_x$ (x=1, 2, 3, 4……) is defined as the relative translational shift of Pd_{Pd2Se3} and $Pd_{PdSe2,}$ indicated by the green circles in Figure 7f-h. In the long-range, the periodical lattice mismatch ($\delta_4 > \delta_3 > \delta_2 > \delta_1$) gives rise to variant Moiré patterns. Figure 7i shows an example of type III heteroepitaxy but with rotational alignment. 2D FFT in Figure 7j shows a θ=45° between the principal diffraction spots $(020)_{Pd2Se3}$ and $(020)_{O\text{-}PdSe2,}$ where the $(110)_{Pd2Se3}$,$(200)_{O\text{-}PdSe2,}$ $(210)_{O\text{-}PdSe2}$ and $(220)_{O\text{-}PdSe2}$ were also clearly displayed. Figure 7k presents the magnified experimental ADF-STEM image showing the Moiré pattern, and the multislice simulated image and atomic models (Figure 7l-q) are in excellent agreement.

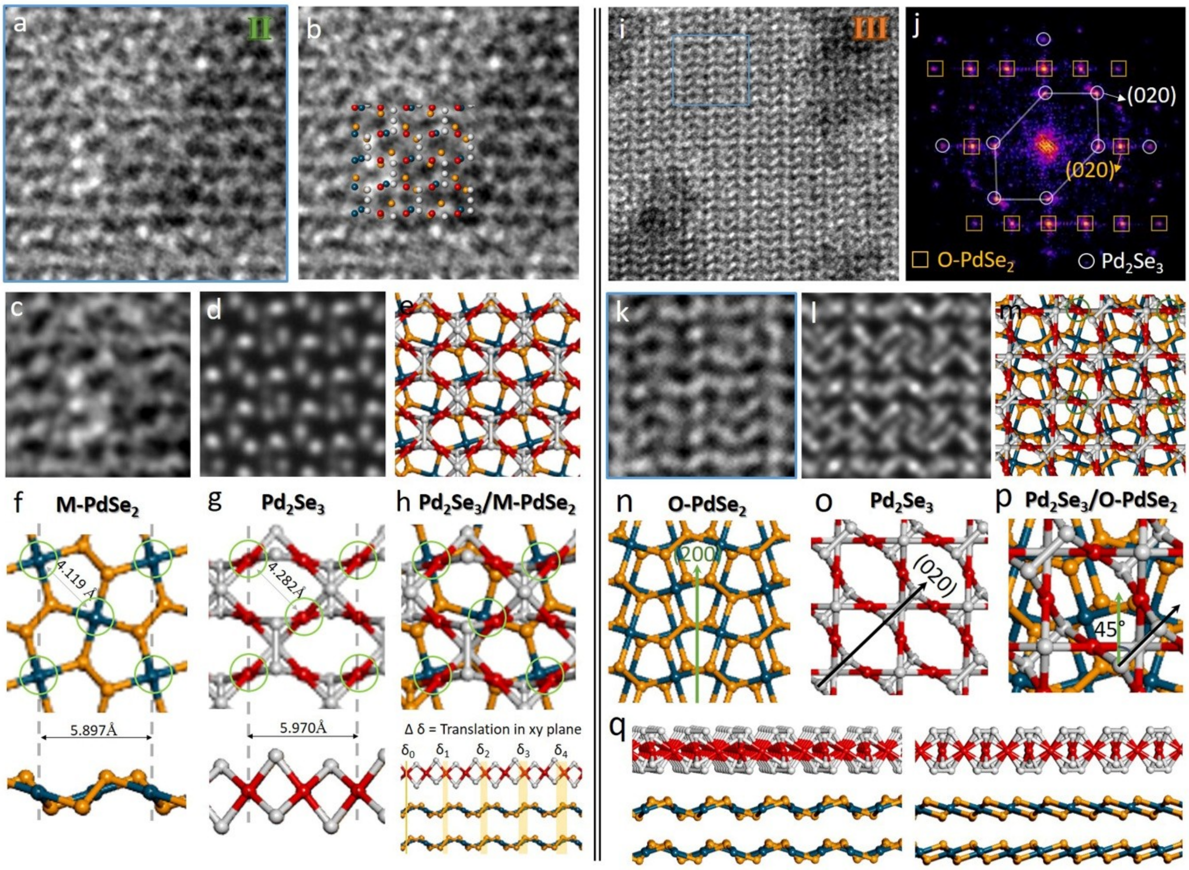

Figure 7. The atomic structures in regions II and III consist of $PdSe_2$ and Pd_2Se_3. (a-h) The Pd_2Se_3/ M-$PdSe_2$ structure in region II. (a-b) ADF-STEM image showing atomic structures of the Pd_2Se_3 and bilayer M-$PdSe_2$. (c) The magnified view of the experimental ADF-STEM image of (a). (d) The multislice simulated ADF-STEM image and (e) corresponding atomic model. (f-h) Atomic models with atomic distances showing the stacking configuration. (i-q) The Pd_2Se_3/O-$PdSe_2$ structure represents region III. (i) ADF-STEM image showing atomic structures of the Pd_2Se_3 and bilayer O-$PdSe_2$. (j) FFT of (i) showing its rotational alignment. (k) The magnified view of the experimental ADF-STEM image of (i). (l) The multislice simulated ADF-STEM image and (m) corresponding atomic model. (n-q) Atomic models with plane direction showing the stacking configuration.

The semiconductor/metal 2D heterostructures of $PdSe_2$/Graphene and Pd_2Se_3/Graphene was demonstrated in Figure 1-7. These then spark our interest in the viability of growth on TMDs semiconductor substrates. Figure 8a displayed the 8mM sample that was selenized for one hour in the identical furnace settings. By comparison with the continuous film growth on graphene, the results show nanoflakes growth of palladium selenide on MoS_2 with the size around few to one hundred nanometers. Figure 8b shows the large-area single domain Pd_2Se_3 on bilayer MoS_2, where the inset shows the Pd_2Se_3 lattice extracted by applying a mask to 2D FFT (Figure 8c) to exclude the MoS_2 reflexes. Furthermore, 2D FFT in Figure 8c indicates that the $(020)_{Pd2Se3}$ aligned with MoS_2 armchair direction. Detailed heteroepitaxy was shown in Figure 8d, confirmed by multislice ADF-STEM image simulation and atomic model in Figure 8e-f. It should be highlighted that two motifs of Pd_2Se_3 have been reported, the connected bulgy rectangle structure and the triangular-shaped with one straight line structure. The former is considered as the innate structure, whereas the latter is often experimentally observed. Intriguingly, both the Pd_2Se_3 nanoflakes grown on graphene (Figure 3c-d and Figure 4) or MoS_2 in our study exhibited the triangular-shaped structure. To understand why the Pd_2Se_3 adopted the triangular-shaped structure when grown on the 2D hexagonal substrates, we compared the Moiré patterns formed from MoS_2 and two structures of Pd_2Se_3. In Figure S15a-b, the atomic models display that the triangular-shaped structure has the shorter spacing between Pd atoms along $[020]_{Pd2Se3}$ direction. In long-range commensurability, the triangular-shaped structure shows a higher lattice match on zigzag directions of 2D hexagons, illustrated by the relative lattice spacing between these two structures on MoS_2 (Figure S15c-h). Notably, the size of Pd_2Se_3 grown on graphene is smaller than that on MoS_2. This could be limited by the surrounding Pd precursors (0.1M). On the other hand, although these two substrates (Graphene(C), MoS_2) are both 2D flat substrate without surface dangling bonds, the vdW interactions between Pd-Se-C and Pd-Se-Mo-S are different, which is generally described by the modified Lennard-Jones potential model.[50, 51] This leads to the different surface diffusion energy for adsorbed species. Moreover, the lattice mismatch between graphene and Pd_2Se_3 are larger than that between MoS_2 and Pd_2Se_3, which could give rise to larger strain energy and surface binding energy for the incorporation of species into Pd_2Se_3 lattice on graphene. Figure 8g shows a monolayer O-$PdSe_2$ on monolayer MoS_2 with inset the extracted $PdSe_2$ lattice. 2D FFT in Figure 8h points out that $(020)_{PdSe2}$ overlapped with the $(100)_{MoS2,}$ denoting the alignment of $(020)_{PdSe2}$ on MoS_2 zigzag direction. The magnified image was shown in Figure 8i, with its heteroepitaxial alignment confirmed by Figure 8i-k.

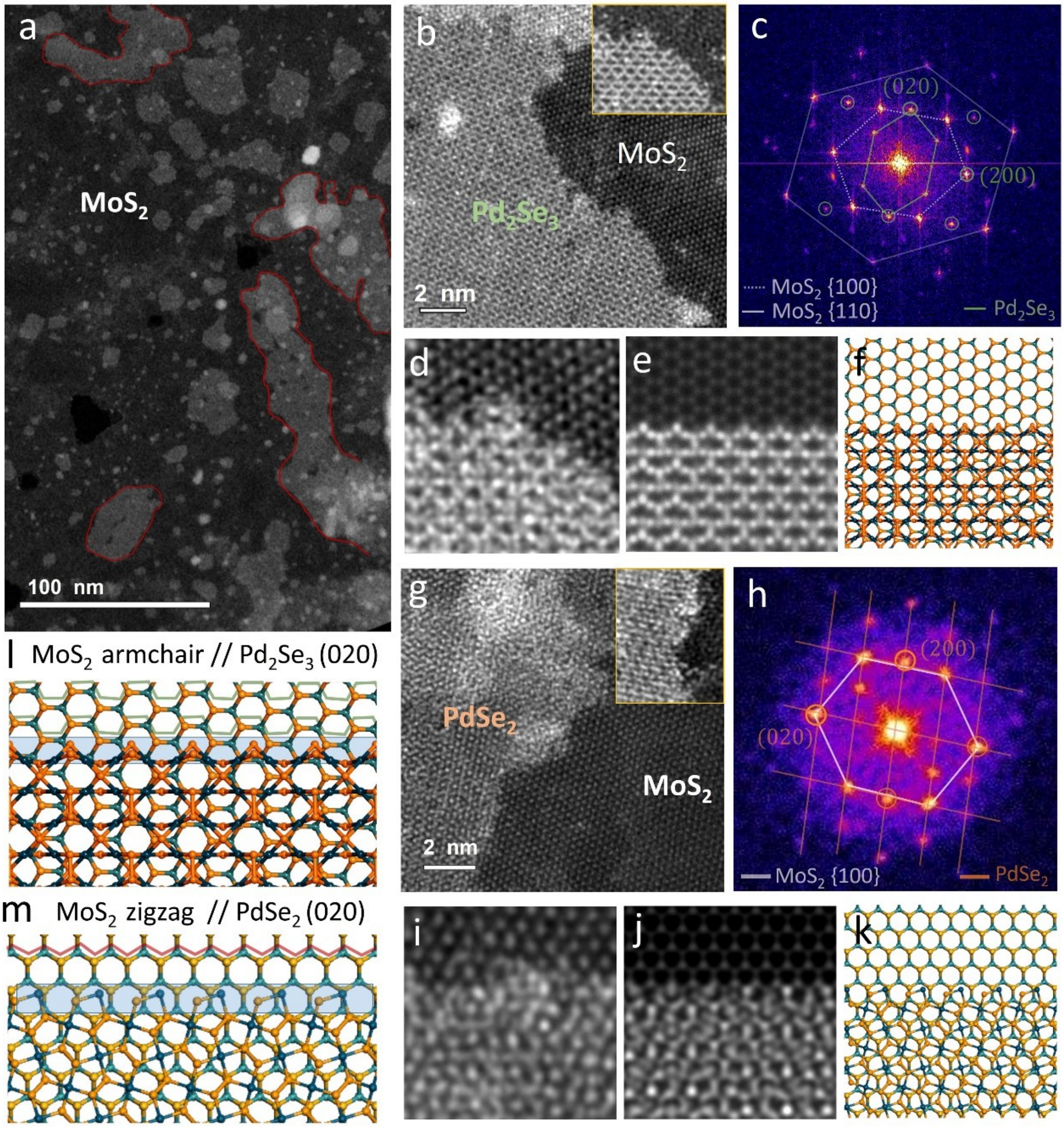

Figure 8. 2D PdSe$_2$/MoS$_2$ and Pd$_2$Se$_3$/MoS$_2$ heterostructures and its epitaxial alignment. (a) Overview of the sizeable 2D palladium selenide grown on MoS$_2$ with bright contrast region marked by a red line showing the morphology of palladium selenide. (b) ADF-STEM image showing the atomic structure of Pd$_2$Se$_3$ grown on bilayer MoS$_2$ and the corresponding FFT (c). (d) Magnified view showing the interface of MoS$_2$/Pd$_2$Se$_3$. (e) Multislice simulated image of

MoS_2/Pd_2Se_3 heterostructure and its atomic model (f). (g) ADF-STEM image showing the atomic structure of $PdSe_2$ grown on monolayer MoS_2 and the corresponding FFT (h). (i) Magnified view showing the monolayer region of a bilayer $PdSe_2$ unit cell grown on monolayer MoS_2. (j) Multislice simulated image of a monolayer $PdSe_2$ on monolayer MoS_2 and its atomic model (k). (l-m) Atomic illustration showing the preferable epitaxial alignment of $PdSe_2/MoS_2$ and Pd_2Se_3/MoS_2 heterostructures.

Figure 9a-b presents a schematic illustration of the selenizing process from the top-view and the side view, depicting the evolution of film growth from pre-seeded precursors. The phase evolution is shown in the diagram of Figure 9c, which is based on the theory of kinetic *versus* thermodynamic reaction control. In principle, kinetic control favors shorter reaction time and lower temperature, whereas thermodynamic control occurs for longer reaction times and higher temperatures. The experimental results in the sample with one-hour selenization only showed the presence of bilayer O-$PdSe_2$ and monolayer Pd_2Se_3, which concurs with the previous findings. These two phases are arguably the thermodynamic-control product under a sufficiently long timescale. Comparatively, the monolayers M-$PdSe_2$ experimentally shown in the 15 min sample, for instance, the bilayer in Figure 6c and trilayers in Figure 6l, is the kinetic-control product. Such phase variations that exhibited features as a function of time can also be described by the state-to-state dynamics, where the monolayers M-$PdSe_2$ with translational stacking was at the states that has lower activation energy whereas the bilayer O-$PdSe_2$ has higher activation energy.

Quantitative kinetic pathway of phase evolution can be further simulated by kinetic Monte Carlo method, in which each state corresponds to one structural motif of interlayer stacking with a energy basin.[51, 52]

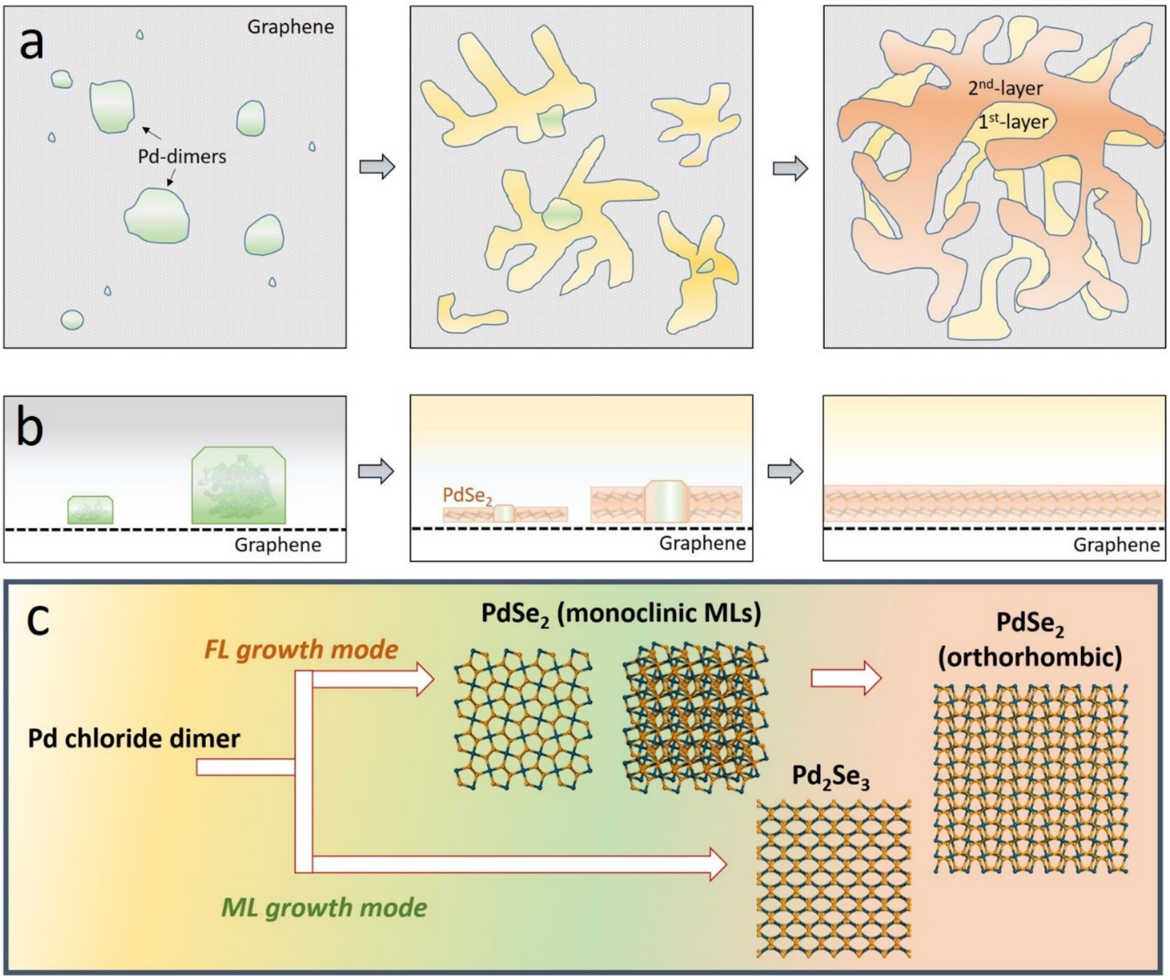

Figure 9. The schematic illustration of growth mechanisms. (a) (b)The illustration from top and side view showing how the Pd-dimers extended to form the continuous 2D film. (c) The diagram showing the phase evolution .

Conclusion

The lack of practical approaches to systematically fabricate 2D materials hinders their integration into the current technology industry. It appears that too often, the fundamental knowledge is missing regarding precursor selection, nucleation placement, growth evolution, and substrate impact. This study provided microscopic characterization of growth in nanoscale, and insights of the kinetic phases and interlayer epitaxy at the atomic level. Equivalently significant, we established a selenization process with the merits of low-temperature, one-step growth that accomplished excellent coverage using pre-deposited precursors. The tunable nucleation of precursors was developed through a simple solution-based process using transition-metal allyl dimers. Few-layer $PdSe_2$ and monolayer Pd_2Se_3 were robustly produced in different precursor concentrations and growth duration. Monolayers M-$PdSe_2$ were favored under kinetic control reaction; however, the bilayer M-$PdSe_2$ existed in AA stacking whereas the trilayer M-$PdSe_2$ exhibited a translational stacking. Interestingly, Pd_2Se_3 adopted the triangular structure with a shorter spacing between Pd atoms. This indicated the increase of commensurability in lattice spacing between Pd_2Se_3 and substrates. In summary, this research has broadened the scope of 2D $PdSe_2$ and Pd_2Se_3 for future applications. Although it is a long way to wafer-scale achievement, we directly synthesized pentagonal materials on hexagonal substrates as 2D van der Waals structures. Further predictive growth models, uniform precursor-distribution strategies, and exploitation of other transition metal complexes can be incorporated in the mono-bi-layer regime to accomplish the industrial-level synthesis.

Methods

Transfer of Graphene and MoS_2 Grown by Chemical Vapor Deposition on TEM grid

Graphene was grown on the copper foil substrate using a 4 inch CVD system. The as-grown sample was coated with polymethyl methacrylate (PMMA) at 4500 rpm for 60 s, followed by heating at 180 ℃ for 1 min, and was then etched in 0.3 M aqueous ammonium persulfate solution. After the copper foil was completely etched away, the PMMA/Graphene layer was rinsed in DI water several times to remove the residue. MoS_2 growth was performed on SiO_2/Si substrate in a two-zone furnace. The system went with Ar gas flow and used molybdenum trioxide and sulfur powder as precursors. The MoS_2 was coated with PMMA at 4500 rpm for 60 s and was baked slightly at 180 ℃ for 1min. In contrast to graphene, MoS_2 was etched in 1 M KOH until the substrate was detached. The floating PMMA/2D layers were then pasted onto clean TEM grids and was baked at 180 ℃ for 30 min to enhance adhesion. Afterward, the PMMA supporting layer was removed by immersing the sample in acetone for 12 hours. The TEM grids containing suspended graphene were cleaned by Ar/H_2 and vacuum annealing while those with suspended MoS_2 were cleaned by vacuum annealing.

Precursor Solution

Allypalladium (II) chloride dimer ($C_6H_{10}Cl_2Pd_2$, ≥98.0%, Sigma-Aldrich) powder was dissolved in 1,2-Dichloroethane to form solutions of concentration 0.1 mM, 1 mM, 8 mM and 20 mM (millimolar). These solutions were sonicated in a room-temperature ultrasonic water bath

(Ultrasonics output of 200 W; peak power of 600 W; operating frequency 30-40 kHz) for 30 min to ensure the agitation and dispersion of nanoparticles. Subsequently, the supernatant of each solution was extracted for drop-casting on graphene/MoS_2 on TEM grids. All solutions with different concentrations were extracted 5 min after being taken out from the ultrasonic bath.

Selenization Settings

A two-furnace CVD system with a 1-inch quartz tube was used to create separate temperature control of selenium source and precursor substrates (TEM grids). The Ar gas flow is used as the carrier gas. For a typical selenizing process, 80 mg of selenium powder (Se, powder, ≥99.5%, Sigma-Aldrich) was placed in the center of Zone 1 at 240 ℃. The TEM grids with precursors on graphene were placed downstream at the center of Zone 2 at 360 ℃.

Characterization of continuous $PdSe_2$ films

Raman analysis was conducted in LabRAM ARAMIS Raman spectrometer system, using 532 nm laser with 100 x objective lens. The areas analyzed are with 5 μm intervals.

Scanning Transmission Electron Microscopy

Annular dark-field scanning transmission electron microscopy was performed at an accelerating voltage of 80 kV, using JEOL ARM200F. Dwell times of 10-20 μs, beam current of 35 pA, and a pixel size of 0.006 nm px^{-1} were used for imaging, with a convergence semi-angle of 25.5 mrad and collecting inner-outer angles 68-275 mrad. For Figure 4 and the EDX in supporting information, a JEOL neoARM was used at 80kV, located in the Texas Materials Institute at the University of Texas at Austin.

Image Processing and Simulations

Images were partly processed with the Image J software using a Gaussian blur filter of 1-2 to reduce noise and a LUT Fire effect to enhance the vision of atoms. Pd_2Se_3 and $PdSe_2$ crystal structures and simulated diffraction were established using Crystal Maker and Single Crystal. Atomic models were constructed *via* Accelrys Discovery Studio Visualizer. Multislice image simulations were performed using JEMS, with the chromatic aberration (C_c) and spherical aberration (Cs) parameters of 0.890 mm and -0.001mm, respectively. The angle range for dark-field imaging was from 70-200 mrad. The defocus for the graphene samples and the MoS_2 samples were set at -2.6 nm and -7.0 nm, respectively.

Associated Content

The authors declare no competing financial interest.

Supporting Information

The Supporting Information is available free of charge on the ACS Publications website at DOI:

Further details of precursor distributions of different concentration before selenization process, growth features corresponding to different concentration, ADF-STEM images of the commercial sample, structural analysis of the area adjacent to the seeds, phase models of M-$PdSe_2$ and O-

$PdSe_2$, another example for the kinetic products, the commensurate lattice of Pd_2Se_3 on substrates, images of growth results under sulfurization.

Author Information

Corresponding Author

Jamie Warner (E-mail: jamie.warner@austin.utexas.edu), Wen-Wei Wu (E-mail: wwwu@mail.nctu.edu.tw)

ORCID

Jamie H. Warner: 0000-0002-1271-2019

Wen-Wei Wu: 0000-0002-8388-8417

Acknowledgment

K.L.T thanks the support from the Graduate Students Study Abroad Program sponsored by the Ministry of Science and Technology, Taiwan (R.O.C.), and the scholarship granted by Taiwan Semiconductor Manufacturing Company (TSMC). This work was also financially supported by the “Center for the Semiconductor Technology Research” from The Featured Areas Research Center Program within the framework of the Higher Education Sprout Project by the Ministry of Education (MOE) in Taiwan. Also supported in part by the Ministry of Science and Technology, Taiwan, under Grant MOST 109-2634-F-009-029.

References

1. Friedrich, J.; von Ammon, W.; Müller, G., 2 - Czochralski Growth of Silicon Crystals. In *Handbook of Crystal Growth (Second Edition)*, Rudolph, P., Ed. Elsevier: Boston, **2015**; pp 45-104.
2. Theis, T. N.; Wong, H.-S. P., The End of Moore's Law: A New Beginning for Information Technology. *Comput. Sci. Eng.* **2017,** *19*, 41-50.
3. Akinwande, D.; Huyghebaert, C.; Wang, C.-H.; Serna, M. I.; Goossens, S.; Li, L.-J.; Wong, H. S. P.; Koppens, F. H. L., Graphene and Two-Dimensional Materials for Silicon Technology. *Nature* **2019,** *573*, 507-518.
4. Wang, H.; Liu, F.; Fu, W.; Fang, Z.; Zhou, W.; Liu, Z., Two-Dimensional Heterostructures: Fabrication, Characterization, and Application. *Nanoscale* **2014,** *6*, 12250-12272.
5. Novoselov, K. S.; Mishchenko, A.; Carvalho, A.; Castro Neto, A. H., 2D Materials and van der Waals Heterostructures. *Science* **2016,** *353*, aac9439.
6. Khan, K.; Tareen, A. K.; Aslam, M.; Wang, R.; Zhang, Y.; Mahmood, A.; Ouyang, Z.; Zhang, H.; Guo, Z., Recent Developments in Emerging Two-Dimensional Materials and Their Applications. *J. Mater. Chem. C* **2020,** *8*, 387-440.
7. Manzeli, S.; Ovchinnikov, D.; Pasquier, D.; Yazyev, O. V.; Kis, A., 2D Transition Metal Dichalcogenides. *Nat. Rev. Mater.* **2017,** *2*, 17033.
8. Zhou, Y.; Xu, W.; Sheng, Y.; Huang, H.; Zhang, Q.; Hou, L.; Shautsova, V.; Warner, J. H.; Symmetry Controlled Reversible Photovoltaic Current Flow in Ultrathin All 2D Vertical Stacked Graphene:MoS2:WS2:Graphene Devices, *ACS Appl. Mater. Inter.* **2019**, 11, 2234-2242
9. Liu, Y.; Zhang, S.; He, J.; Wang, Z. M.; Liu, Z., Recent Progress in the Fabrication, Properties, and Devices of Heterostructures Based on 2D Materials. *Nano-Micro Lett.* **2019,** *11*, 13.
10. Wang, H.; Li, C.; Fang, P.; Zhang, Z.; Zhang, J. Z., Synthesis, Properties, and Optoelectronic Applications of Two-Dimensional MoS2 and MoS2-based Heterostructures. *Chem. Soc. Rev.* **2018,** *47*, 6101-6127.
11. Wang, S.; Robertson, A.; Warner, J. H., Atomic Structure of Defects and Dopants in 2D Layered Transition Metal Dichalcogenides. *Chem. Soc. Rev.* **2018,** *47*, 6764-6794.
12. Kim, S.-Y.; Kwak, J.; Ciobanu, C. V.; Kwon, S.-Y., Recent Developments in Controlled Vapor-Phase Growth of 2D Group 6 Transition Metal Dichalcogenides. *Adv. Mater.* **2019,** *31*, 1804939.
13. Chen, T.-A.; Chuu, C.-P.; Tseng, C.-C.; Wen, C.-K.; Wong, H. S. P.; Pan, S.; Li, R.; Chao, T.-A.; Chueh, W.-C.; Zhang, Y.; Fu, Q.; Yakobson, B. I.; Chang, W.-H.; Li, L.-J., Wafer-Scale Single-Crystal Hexagonal Boron Nitride Monolayers on Cu (111). *Nature* **2020,** *579*, 219-223.
14. Bhimanapati, G. R.; Lin, Z.; Meunier, V.; Jung, Y.; Cha, J.; Das, S.; Xiao, D.; Son, Y.; Strano, M. S.; Cooper, V. R.; Liang, L.; Louie, S. G.; Ringe, E.; Zhou, W.; Kim, S. S.; Naik, R. R.; Sumpter, B. G.; Terrones, H.; Xia, F.; Wang, Y., *et al*. Recent Advances in Two-Dimensional Materials beyond Graphene. *ACS Nano* **2015,** *9*, 11509-11539.
15. Gong, C.; Zhang, X., Two-Dimensional Magnetic Crystals and Emergent Heterostructure Devices. *Science* **2019,** *363*, eaav4450.

16. Zhou, J.; Lin, J.; Huang, X.; Zhou, Y.; Chen, Y.; Xia, J.; Wang, H.; Xie, Y.; Yu, H.; Lei, J.; Wu, D.; Liu, F.; Fu, Q.; Zeng, Q.; Hsu, C.-H.; Yang, C.; Lu, L.; Yu, T.; Shen, Z.; Lin, H., *et al*. A Library of Atomically Thin Metal Chalcogenides. *Nature* **2018,** *556*, 355-359.

17. Molle, A.; Grazianetti, C.; Tao, L.; Taneja, D.; Alam, M. H.; Akinwande, D., Silicene, Silicene Derivatives, and Their Device Applications. *Chem. Soc. Rev.* **2018,** *47*, 6370-6387.

18. Geng, D.; Yang, H. Y., Recent Advances in Growth of Novel 2D Materials: Beyond Graphene and Transition Metal Dichalcogenides. *Adv. Mater.* **2018,** *30*, 1800865.

19. Wang, Y.; Li, L.; Yao, W.; Song, S.; Sun, J. T.; Pan, J.; Ren, X.; Li, C.; Okunishi, E.; Wang, Y.-Q.; Wang, E.; Shao, Y.; Zhang, Y. Y.; Yang, H.-t.; Schwier, E. F.; Iwasawa, H.; Shimada, K.; Taniguchi, M.; Cheng, Z.; Zhou, S., *et al*. Monolayer PtSe2, a New Semiconducting Transition-Metal-Dichalcogenide, Epitaxially Grown by Direct Selenization of Pt. *Nano Lett.* **2015,** *15*, 4013-4018.

20. Pi, L.; Li, L.; Liu, K.; Zhang, Q.; Li, H.; Zhai, T., Recent Progress on 2D Noble-Transition-Metal Dichalcogenides. *Adv. Funct. Mater.* **2019,** *29*, 1904932.

21. Zeng, L.-H.; Wu, D.; Lin, S.-H.; Xie, C.; Yuan, H.-Y.; Lu, W.; Lau, S. P.; Chai, Y.; Luo, L.-B.; Li, Z.-J.; Tsang, Y. H., Controlled Synthesis of 2D Palladium Diselenide for Sensitive Photodetector Applications. *Adv. Funct. Mater.* **2019,** *29*, 1806878.

22. Chow, W. L.; Yu, P.; Liu, F.; Hong, J.; Wang, X.; Zeng, Q.; Hsu, C.-H.; Zhu, C.; Zhou, J.; Wang, X.; Xia, J.; Yan, J.; Chen, Y.; Wu, D.; Yu, T.; Shen, Z.; Lin, H.; Jin, C.; Tay, B. K.; Liu, Z., High Mobility 2D Palladium Diselenide Field-Effect Transistors with Tunable Ambipolar Characteristics. *Adv. Mater.* **2017,** *29*, 1602969.

23. Zhang, G.; Amani, M.; Chaturvedi, A.; Tan, C.; Bullock, J.; Song, X.; Kim, H.; Lien, D.-H.; Scott, M. C.; Zhang, H.; Javey, A., Optical and Electrical Properties of Two-Dimensional Palladium Diselenide. *Appl. Phys. Lett.* **2019,** *114*, 253102.

24. Long, M.; Wang, Y.; Wang, P.; Zhou, X.; Xia, H.; Luo, C.; Huang, S.; Zhang, G.; Yan, H.; Fan, Z.; Wu, X.; Chen, X.; Lu, W.; Hu, W., Palladium Diselenide Long-Wavelength Infrared Photodetector with High Sensitivity and Stability. *ACS Nano* **2019,** *13*, 2511-2519.

25. Gu, Y.; Cai, H.; Dong, J.; Yu, Y.; Hoffman, A. N.; Liu, C.; Oyedele, A. D.; Lin, Y.-C.; Ge, Z.; Puretzky, A. A.; Duscher, G.; Chisholm, M. F.; Rack, P. D.; Rouleau, C. M.; Gai, Z.; Meng, X.; Ding, F.; Geohegan, D. B.; Xiao, K., Two-Dimensional Palladium Diselenide with Strong In-Plane Optical Anisotropy and High Mobility Grown by Chemical Vapor Deposition. *Adv. Mater.* **2020**, 1906238.

26. Oyedele, A. D.; Yang, S.; Liang, L.; Puretzky, A. A.; Wang, K.; Zhang, J.; Yu, P.; Pudasaini, P. R.; Ghosh, A. W.; Liu, Z.; Rouleau, C. M.; Sumpter, B. G.; Chisholm, M. F.; Zhou, W.; Rack, P. D.; Geohegan, D. B.; Xiao, K., PdSe2: Pentagonal Two-Dimensional Layers with High Air Stability for Electronics. *J. Am. Chem. Soc.* **2017,** *139*, 14090-14097.

27. Lin, J.; Zuluaga, S.; Yu, P.; Liu, Z.; Pantelides, S. T.; Suenaga, K., Novel Pd2Se3 Two-Dimensional Phase Driven by Interlayer Fusion in Layered PdSe2. *Phys. Rev. Lett.* **2017,** *119*, 016101.

28. Molle, A.; Goldberger, J.; Houssa, M.; Xu, Y.; Zhang, S.-C.; Akinwande, D., Buckled Two-Dimensional Xene Sheets. *Nat. Mater.* **2017,** *16*, 163-169.

29. Qin, D.; Yan, P.; Ding, G.; Ge, X.; Song, H.; Gao, G., Monolayer PdSe2: A Promising Two-Dimensional Thermoelectric Material. *Sci. Rep.* **2018,** *8*, 2764.

30. Chen, J.; Ryu, G. H.; Sinha, S.; Warner, J. H., Atomic Structure and Dynamics of Defects and Grain Boundaries in 2D Pd2Se3 Monolayers. *ACS Nano* **2019,** *13*, 8256-8264.

31. Zhu, X.; Li, F.; Wang, Y.; Qiao, M.; Li, Y., Pd2Se3 Monolayer: A Novel Two-Dimensional Material with Excellent Electronic, Transport, and Optical Properties. *J. Mater. Chem. C* **2018,** *6*, 4494-4500.

32. Naghavi, S. S.; He, J.; Xia, Y.; Wolverton, C., Pd2Se3 Monolayer: A Promising Two-Dimensional Thermoelectric Material with Ultralow Lattice Thermal Conductivity and High Power Factor. *Chem. Mater.* **2018,** *30*, 5639-5647.

33. Li, X.; Zhang, S.; Guo, Y.; Wang, F. Q.; Wang, Q., Physical Properties and Photovoltaic Application of Semiconducting Pd_2Se_3 Monolayer. *Nanomaterials* **2018,** *8*, 832.

34. Briggs, N.; Subramanian, S.; Lin, Z.; Li, X.; Zhang, X.; Zhang, K.; Xiao, K.; Geohegan, D.; Wallace, R.; Chen, L.-Q.; Terrones, M.; Ebrahimi, A.; Das, S.; Redwing, J.; Hinkle, C.; Momeni, K.; van Duin, A.; Crespi, V.; Kar, S.; Robinson, J. A., A Roadmap for Electronic Grade 2D Materials. *2D Mater.* **2019,** *6*, 022001.

35. Shi, Y.; Li, H.; Li, L.-J., Recent Advances in Controlled Synthesis of Two-Dimensional Transition Metal Dichalcogenides *via* Vapour Deposition Techniques. *Chem. Soc. Rev.* **2015,** *44*, 2744-2756.

36. Lee, Y.-H.; Zhang, X.-Q.; Zhang, W.; Chang, M.-T.; Lin, C.-T.; Chang, K.-D.; Yu, Y.-C.; Wang, J. T.-W.; Chang, C.-S.; Li, L.-J.; Lin, T.-W., Synthesis of Large-Area MoS2 Atomic Layers with Chemical Vapor Deposition. *Adv. Mater.* **2012,** *24*, 2320-2325.

37. Li, G.; Zhang, Y.-Y.; Guo, H.; Huang, L.; Lu, H.; Lin, X.; Wang, Y.-L.; Du, S.; Gao, H.-J., Epitaxial Growth and Physical Properties of 2D Materials Beyond Graphene: from Monatomic Materials to Binary Compounds. *Chem. Soc. Rev.* **2018,** *47*, 6073-6100.

38. Oyedele, A. D.; Yang, S.; Feng, T.; Haglund, A. V.; Gu, Y.; Puretzky, A. A.; Briggs, D.; Rouleau, C. M.; Chisholm, M. F.; Unocic, R. R.; Mandrus, D.; Meyer, H. M.; Pantelides, S. T.; Geohegan, D. B.; Xiao, K., Defect-Mediated Phase Transformation in Anisotropic Two-Dimensional PdSe2 Crystals for Seamless Electrical Contacts. *J. Am. Chem. Soc.* **2019,** *141*, 8928-8936.

39. Shautsova, V.; Sinha, S.; Hou, L.; Zhang, Q.; Tweedie, M.; Lu, Y.; Sheng, Y.; Porter, B. F.; Bhaskaran, H.; Warner, J. H., Direct Laser Patterning and Phase Transformation of 2D PdSe2 Films for On-Demand Device Fabrication. *ACS Nano* **2019,** *13*, 14162-14171.

40. Lei, W.; Cai, B.; Zhou, H.; Heymann, G.; Tang, X.; Zhang, S.; Ming, X., Ferroelastic Lattice Rotation and Band-Gap Engineering in Quasi 2D Layered-Structure PdSe2 under Uniaxial Stress. *Nanoscale* **2019,** *11*, 12317-12325.

41. Liang, Q.; Zhang, Q.; Gou, J.; Song, T.; Arramel; Chen, H.; Yang, M.; Lim, S. X.; Wang, Q.; Zhu, R.; Yakovlev, N.; Tan, S. C.; Zhang, W.; Novoselov, K. S.; Wee, A. T. S., Performance Improvement by Ozone Treatment of 2D PdSe2. *ACS Nano* **2020,** *14*, 5668-5677.

42. Ryu, G. H.; Zhu, T.; Chen, J.; Sinha, S.; Shautsova, V.; Grossman, J. C.; Warner, J. H., Striated 2D Lattice with Sub-nm 1D Etch Channels by Controlled Thermally Induced Phase Transformations of PdSe2. *Adv. Mater.* **2019,** *31*, 1904251.

43. Nguyen, G. D.; Oyedele, A. D.; Haglund, A.; Ko, W.; Liang, L.; Puretzky, A. A.; Mandrus, D.; Xiao, K.; Li, A.-P., Atomically Precise PdSe2 Pentagonal Nanoribbons. *ACS Nano* **2020,** *14*, 1951-1957.

44. Li, E.; Wang, D.; Fan, P.; Zhang, R.; Zhang, Y.-Y.; Li, G.; Mao, J.; Wang, Y.; Lin, X.; Du, S.; Gao, H.-J., Construction of Bilayer PdSe2 on Epitaxial Graphene. *Nano Res.* **2018,** *11*, 5858-5865.

45. Lu, L.-S.; Chen, G.-H.; Cheng, H.-Y.; Chuu, C.-P.; Lu, K.-C.; Chen, C.-H.; Lu, M.-Y.; Chuang, T.-H.; Wei, D.-H.; Chueh, W.-C.; Jian, W.-B.; Li, M.-Y.; Chang, Y.-M.; Li, L.-J.; Chang, W.-H., Layer-Dependent and In-Plane Anisotropic Properties of Low-Temperature Synthesized Few-Layer PdSe2 Single Crystals. *ACS Nano* **2020**.

46. Xu, W.; Jiang, J.; Ma, H.; Zhang, Z.; Li, J.; Zhao, B.; Wu, R.; Yang, X.; Zhang, H.; Li, B.; Shu, W.; Zhang, Z.; Li, B.; Liu, Y.; Liao, L.; Duan, X., Vapor Phase Growth of Two-Dimensional PdSe2 Nanosheets for High-Photoresponsivity Near-Infrared Photodetectors. *Nano Research* **2020**.

47. Dong, J.; Zhang, L.; Ding, F., Kinetics of Graphene and 2D Materials Growth. *Adv. Mater.* **2019,** *31*, 1801583.

48. Liu, K.-K.; Zhang, W.; Lee, Y.-H.; Lin, Y.-C.; Chang, M.-T.; Su, C.-Y.; Chang, C.-S.; Li, H.; Shi, Y.; Zhang, H.; Lai, C.-S.; Li, L.-J., Growth of Large-Area and Highly Crystalline MoS2 Thin Layers on Insulating Substrates. *Nano Lett.* **2012,** *12*, 1538-1544.

49. Sinha, S.; Zhu, T.; France-Lanord, A.; Sheng, Y.; Grossman, J. C.; Porfyrakis, K.; Warner, J. H., Atomic Structure and Defect Dynamics of Monolayer Lead Iodide Nanodisks with Epitaxial Alignment on Graphene. *Nat. Commun.* **2020,** *11*, 823.

50. Rappe, A. K.; Casewit, C. J.; Colwell, K. S.; Goddard, W. A.; Skiff, W. M., UFF, A Full Periodic Table Force Field for Molecular Mechanics and Molecular Dynamics Simulations. *J. Am. Chem. Soc.* **1992,** *114*, 10024-10035.

51. Momeni, K.; Ji, Y.; Wang, Y.; Paul, S.; Neshani, S.; Yilmaz, D. E.; Shin, Y. K.; Zhang, D.; Jiang, J.-W.; Park, H. S.; Sinnott, S.; van Duin, A.; Crespi, V.; Chen, L.-Q., Multiscale Computational Understanding and Growth of 2D Materials: A Review. *npj Comput. Mater.* **2020,** *6*, 22.

52. Voter, A. F. In *Introduction to the Kinetic Monte Carlo Method*, Dordrecht, Springer Netherlands: Dordrecht, **2007**; pp 1-23.

TOC graphic

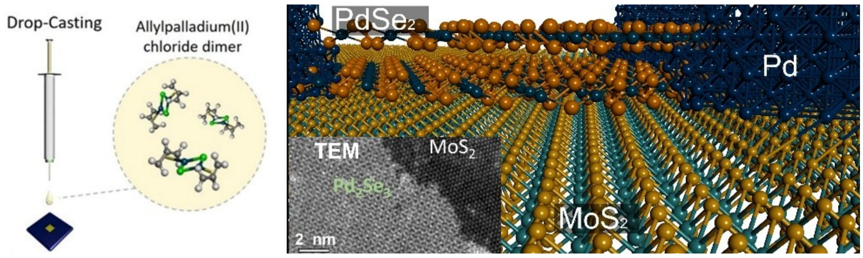
Drop-Casting
Allylpalladium(II) chloride dimer
PdSe$_2$
Pd
TEM
MoS$_2$
Pd$_2$Se$_3$
2 nm
MoS$_2$